

This is the **submitted version** of the journal article:

Yang, Dawei; Liang, Zhifu; Zhang, Chaoqi; [et al.]. «NbSe₂ meets C₂N : a 2D-2D heterostructure catalysts as multifunctional polysulfide mediator in ultra-long-life lithium-sulfur batteries». *Advanced Energy Materials*, Vol. 11, issue 36 (Sep. 2021), art. 2101250. DOI 10.1002/aenm.202101250

This version is available at <https://ddd.uab.cat/record/271951>

under the terms of the  ^{IN} COPYRIGHT license

NbSe₂ Meets C₂N: A 2D-2D Heterostructure Catalysts as Multifunctional Polysulfide Mediator in Ultra-Long-Life Lithium– Sulfur Batteries

Dawei Yang, Chaoqi Zhang, Zhifu Liang, Jordi Jacas Biendicho, Marc Botifoll, Maria Chiara Spadaro, Qiulin Chen, Mengyao Li, Alberto Ramon, Ahmad Ostovari Moghaddam, Jordi Llorca, Jia-ao Wang*, Joan Ramon Morante, Jordi Arbiol, Andreu Cabot*

D. W. Yang, C. Q. Zhang, Z. F. Liang, M. Y. Li, A. Ramon, Dr. J. J. Biendicho, Prof. J. R. Morante, Prof. A. Cabot

*Catalonia Institute for Energy Research - IREC,
Sant Adrià de Besòs, Barcelona, 08930, Spain
Email: acabot@irec.cat*

*D. W. Yang, C. Q. Zhang, M. Y. Li, A. Ramon, Prof. J. R. Morante
Department of Electronic and Biomedical Engineering
Universitat de Barcelona, 08028 Barcelona, Spain*

*Z. F. Liang, M. Botifoll, Dr. M. C. Spadaro, Prof. J. Arbiol
Catalan Institute of Nanoscience and Nanotechnology (ICN2)
CSIC and BIST, Campus UAB, Bellaterra, 08193 Barcelona, Spain*

*Q. L. Chen
State Key Laboratory for Physical Chemistry of Solid Surfaces, Fujian Key Laboratory of Materials
Genome, College of Materials, Xiamen University, Xiamen 361005, China*

*A. O. Moghaddam
South Ural State University, 76, Lenin Ave., Chelyabinsk 454080, Russia*

*Prof. J. Llorca
Institute of Energy Technologies, Department of Chemical Engineering and Barcelona Research
Center in Multiscale Science and Engineering, Universitat Politècnica de Catalunya, EEBE, 08019,
Barcelona, Spain*

*J. A. Wang
School of Material Science and Engineering, University of Jinan, Jinan 250022, China
Department of Renewable Energy, Oak Ridge National Laboratory P.O. Box 2008 Oak Ridge, TN 37831
Email: wangjiaao0720@163.com*

Prof. J. Arbiol, Prof. A. Cabot

ICREA

Pg. Lluís Companys 23, 08010 Barcelona, Spain

Keywords: Niobium selenide, C₂N, nanosheet, lithium polysulfide, lithium-sulfur batteries

Abstract

The shuttle effect and sluggish conversion kinetics of lithium polysulfides (LiPS) hamper the practical application of lithium-sulfur batteries (LSBs). Toward overcoming these limitations, herein we present a multifunctional polysulfide mediator based on a NbSe₂ absorber and Li-S catalyst grown on top of conductive C₂N nanosheets. Density functional theory (DFT) calculations and experimental results demonstrate that C₂N@NbSe₂ forms N-Li and Nb-S chemical bonds to trap LiPS species. Besides, the C₂N framework effectively promotes charge transport, and C₂N/NbSe₂ heterojunctions improve electron transfer and promote the catalytic conversion of LiPS. As a result, LSBs cathodes based on C₂N@NbSe₂/S exhibit a high initial capacity of 1545 mAh g⁻¹ at 0.1C. Even more exciting, C₂N@NbSe₂/S cathodes are characterized by impressive cycling stability with only 0.012% capacity decay per cycle after 2000 cycles at 3 C, maintaining 96.7 % of the 610 mAh g⁻¹ capacity during the last 1500 cycles. Even at a sulfur loading of 5.6 mg cm⁻², a high areal capacity of 5.65 mAh cm⁻² is delivered. These results demonstrate that C₂N@NbSe₂ can act as multifunctional polysulfide mediator to chemically adsorb LiPS, accelerate Li-ion diffusion, chemically catalyze LiPS conversion and lower the energy barrier for Li₂S precipitation/decomposition. These properties make C₂N@NbSe₂ a promising candidate sulfur host in LSB cathodes, which will allow achieving the needs imposed by practical applications.

Introduction

Lithium-sulfur batteries (LSBs) attract enormous interest due to their high theoretical energy density (2600 Wh kg^{-1}) and potential for low-cost.¹⁻³ However, several challenges remain to be overcome to realize their commercial deployment. First, the electrically insulating character of sulfur and lithium sulfide results in a poor charge transport within the cathode, what limits rate capability and sulfur utilization. Besides, intermediate lithium polysulfides (LiPS) dissolve into the electrolyte and migrate from the cathode to the anode. This LiPS diffusion, which is known as the shuttle effect, results in irreversible corrosion of the lithium anode and low Coulombic efficiency.^{4,5} Additionally, large volumetric variations of the sulfur cathode ($\approx 80\%$) during charge/discharge processes lead to poor cycling stability.^{6,7}

To overcome these limitations, huge efforts are being directed toward the development of a sulfur host that provides high electrical conductivity, effectively adsorbs LiPS and rapidly catalyze their redox conversion to solid $\text{Li}_2\text{S}_2/\text{Li}_2\text{S}$, blocking their dissolution, and which is able to accommodate large volume changes without disintegrating.

To improve the electrical conductivity of sulfur cathodes, carbon materials have been extensively studied, including porous carbon,⁸ carbon nanotube,⁹ graphene,¹⁰ nanofibers and covalent organic framework.^{11,12} While carbon materials certainly facilitate electron transport and transfer, their capability to suppress LiPS shuttling is very limited due to the weak interaction of polar LiPS with the nonpolar surface of carbons.^{9,13}

The introduction of nitrogen within the carbon structure can promote interaction with Li and S atoms within LiPS, as demonstrated for $\text{g-C}_3\text{N}_4$ and nitrogen-doped hollow carbon.²² An alternative C-N materials worth to be explored is C_2N . DFT calculations have anticipated C_2N to be an excellent cathode material in LSBs, with some advantages over $\text{g-C}_3\text{N}_4$.^{27,28} C_2N is a two dimensional (2D) graphene-like covalent organic framework (COF) where a hole from the original graphene structure is surrounded by 6 N atoms each with one dangling bond. The size of the hole allows anchoring one S_8 molecule together with few interacting Li atoms. Besides, compared with $\text{g-C}_3\text{N}_4$, the structure of C_2N makes it mechanically more sturdy. Despite the high potential as sulfur host in LSBs theoretically predicted for this material, its real performance remains to be experimentally demonstrated.

On the other hand, several polar materials, e.g. metal oxides,^{13,14} nitrides,¹⁵ and sulfides¹⁶, endow strong dipole-dipole interactions with LiPS. Few of these materials additionally promote the catalytic LiPS redox conversion, which significantly contributes to blocking the shuttle effect.¹⁷ Nevertheless, such polar materials are generally characterized by poor electrical conductivity and moderate surface areas, which limit the electrode rate capability and sulfur utilization.^{18,19}

Transition metal selenides (TMSe) have been proposed as active material in supercapacitors, Zn batteries, and electrolyzers among others, offering relatively high electrical conductivities and excellent catalytic activities.^{20,21} These properties make TMSe also suitable as sulfur hosts in LSBs.^{22,23} Besides TMSe are characterized by polar surfaces to effectively chemisorb LiPS. Among transition metals, Nb-based materials, such as Nb₂O₅ and NbN, have recently received much interest as sulfur hosts in LSBs, in account of their high adsorption capability and notable catalytic activity toward polysulfide conversion.^{24,25} Surprisingly, in spite of its high potential, niobium selenide (NbSe₂) has not been tested as cathode host material in LiPS. NbSe₂ is a polar compound with a two dimensional (2D) crystal structure, and which has been considered for other numerous electrocatalytic reactions.²⁶

In this work, we combine two unexplored materials in the field of LSBs to produce a high-performance sulfur host that is employed as cathode material in LSBs. We first detail the synthesis of C₂N@NbSe₂ nanosheets using a two-step process and thoroughly characterize their structural, chemical and functional properties. Subsequently, the performance of LSBs cathodes based on these nanocomposites is tested. The obtained results are rationalized with the help of density functional theory (DFT) calculations.

Experimental Section

Chemicals: Ethylenediamine (EDA, 99%), hexaketonocyclohexane octahydrate (HACO, 99%), 1,3-dioxolane (DOL, 99.5%), lithium nitrate (LiNO_3 , 99.98%), lithium sulfide (Li_2S , 99.9%), poly(vinylidene fluoride) (PVDF, 99%), Super P (99%), chloroanilic acid (CAA, 98%) and 1-octadecene (ODE, 90%) were purchased from Alfa Aesar. Sulfuric acid (95%~98%), N-methyl-2-pyrrolidone (NMP, 99.99%), diethyl ether (99.9%), niobium(V) chloride (NbCl_5 , 99%), selenium powder (99%), sublimed sulfur (99.98%) and tetraethylene glycol dimethyl ether (99%) were purchased from Sigma-Aldrich. Oleylamine (OAm, approximate C18 content 80-90%), lithium bis(trifluoromethanesulfonyl) imide (LiTFSI, 99%) was purchased from Acros Organics and 1,2-dimethoxymethane (DME, 99%) was from Honeywell. All chemicals were used without further purification.

Synthesis of hexaaminobenzene (HAB): CAA was added into a 15 mL glass vial which was placed in a 0 °C ice bath, under vigorous stirring. Next, 5.64 mL EDA and a few drops of concentrated sulfuric acid were added. Then the ice bath was removed and the obtained solution was warmed up to room temperature. Afterward, the solution was transferred to a 15 mL Teflon autoclave, where it was maintained at 80 °C for 12 h to complete the amination reactions. Then the solution was cooled to room temperature and the obtained mixture was vacuum filtrated using a polytetrafluoroethylene (PTFE) membrane (0.47 μm), rinsed with diethyl ether and degassed ethanol three times, and finally dried until further use.

Synthesis of C_2N : An equal molar ratio of HAB and HACO, and degassed NMP were introduced into a three-necked round bottom flask under argon gas placed in an ice bath. Under vigorous stirring, a few drops of concentrated sulfuric acid were added. Then the ice bath was removed and the mixture was warmed up to room temperature. The resultant solution was heated to 175 °C for 12 h. After cooling to room temperature, the mixture was vacuum filtrated, washed with ethanol and water for three times and freeze-dried for 24 h. Finally, the obtained black solid was annealed at 450 °C for 3 h under argon gas with a ramp rate of 5 °C/min.

Synthesis of $\text{C}_2\text{N}@\text{NbSe}_2$ and NbSe_2 : 15 mL OAm, 2 mL ODE and 10 mL of a C_2N ethanol solution (6 mg ml^{-1}) were added in a three-necked flask and heated to 130 °C for about 30 min under Ar atmosphere to remove water, ethanol and oxygen. Afterward, 1 mmol NbCl_5 and 2 mmol Se powder were added into the solution and the mixture was rapidly heated to 280 °C for

2 h. After cooling, the obtained black product was washed with ethanol and hexane via centrifugation, and then dried in a vacuum oven at 60 °C overnight. As a reference material, NbSe₂ nanosheets were synthesized following the above synthetic protocol but adding no C₂N. *Synthesis of C₂N@NbSe₂/S, NbSe₂/S and C₂N/S:* Host-sulfur composites were obtained through a simple melt diffusion process. In brief, a mixture of the host material (C₂N@NbSe₂, NbSe₂ or C₂N) and sulfur powder with a weight ratio (1:3) was heated at 155 °C for 12 h under Ar atmosphere. The obtained powder was immersed in a 10 mL CS₂ and ethanol solution (1:4, volume ratio) for several times to remove the redundant sulfur not incorporated into the host.

Materials Characterization: Crystal structures were analyzed by X-ray diffraction (XRD) using a Bruker AXS D8 Advance X-ray diffractometer with Cu K radiation ($\lambda = 1.5106 \text{ \AA}$) operating at 40 kV and 40 mA. Scanning electron microscopy analysis was performed on a Zeiss Auriga field emission SEM operating at 20 kV. Transmission electron microscopy (TEM) characterization was carried out on a Zeiss Libra 120 operating at 120 kV. High-resolution TEM (HRTEM), scanning TEM (STEM) and electron energy loss spectroscopy (EELS) composition maps were obtained using a field emission gun FEI Tecnai F20 microscope operated at 200 kV with an embedded Gatan Quantum Spectrometer. X-ray photoelectron spectroscopy (XPS) measurements were carried out using 150 W and a Phoibos 150 MCD-9 detector. The sulfur content within the sulfur cathode composite was tested by thermogravimetric analysis (TGA) on a PerkinElmer Diamond TG/DTA instrument. UV–vis absorption spectra were collected on a PerkinElmer LAMBDA 950 UV–vis spectrophotometer. Nitrogen adsorption-desorption isotherms were recorded on a Tristar II 3020 Micromeritics system. Specific surface areas and pore size distributions were determined by Brunauer–Emmett–Teller (BET) and Barrett-Joyner-Halenda (BJH) methods.

Electrochemical Measurements: To prepare working electrodes, active materials (C₂N@NbSe₂/S, NbSe₂/S and C₂N/S), PVDF binder and Super P were mixed with a mass ratio of 8:1:1 in NMP. The prepared homogeneous slurry was coated on an aluminum foil and vacuum dried at 60 °C overnight. The aluminum foil was then punched into 12 mm disks. The sulfur loading for regular electrodes was around 1 mg cm⁻², but higher loadings of 3.0 and 5.6 mg cm⁻² were also prepared. CR2032-type coin cells were assembled in an Ar-filled glove box with Celgard 2400 membranes as separators, and lithium metal as counter electrode. The

electrolyte used consisted of 1.0 M LiTFSI and contained 0.2 M LiNO₃ solution in DOL and DME (1:1; v:v). The electrolyte/sulfur ratio was typically 20 $\mu\text{L mg}^{-1}$, but decreased to 12 $\mu\text{L mg}^{-1}$ when using cathodes with higher sulfur loadings. To allow enough time for the electrolyte to penetrate the electrode sufficiently, all coin cells were aged for several hours before testing. Galvanostatic charge/discharge measurements were conducted in a voltage window of 1.7-2.8 V vs. Li⁺/Li using a Neware BTS4008 battery tester. Cyclic voltammetry (CV) curves were obtained at operating potentials of 1.7-2.8 V with a scanning rate range from 0.1 to 0.4 mV s⁻¹. Electrochemical impedance spectroscopy (EIS) analyses were performed in the frequency range of 0.01-10⁵ Hz with an amplitude of 10 mV.

Preparation of Li₂S₄ Solution and Adsorption Test: Li₂S₄ solutions were prepared by dissolving sulfur and Li₂S with a molar ratio of 3:1 in DME and DOL (volume ratio of 1:1) under continuous stirring overnight in a glove box. The solution eventually became homogeneous and acquired a dark brown color. To evaluate the polysulfide absorption ability, 20 mg of active materials (C₂N@NbSe₂, NbSe₂ and C₂N) were added to 3.0 mL 10 mM Li₂S₄ solution. The obtained mixtures were vigorously stirred for 2 h and aged overnight.

Measurement of Nucleation and Dissolution of Li₂S: The nucleation and dissolution of Li₂S were measured to investigate the liquid–solid reaction kinetics. A certain amount of C₂N@NbSe₂ (or NbSe₂ or C₂N) dissolved in ethanol was coated on carbon papers used as working electrode. Li foil worked as the counter electrode. A solution containing 20 μL of 0.25 M Li₂S₈ and 1.0 M LiTFSI in tetraethylene glycol dimethyl ether solution was used as catholyte. The anolyte consisted of 20 μL of a 1.0 M LiTFSI solution without Li₂S₈. During the nucleation test, to reduce the generation of higher order LiPS than Li₂S₄, coin cells were initially held at 2.06 V. Subsequently, the cells were held at 2.05 V until current decreased to 0.01 mA to make Li₂S nucleate and grow. To study the Li₂S dissolution, fresh coin cells were assembled. The cells were firstly discharged at a current of 0.10 mA to 1.80 V, following by galvanostatically discharging at 0.01 mA to 1.80 V to fully transform S to solid Li₂S. After this discharge, the cells were potentiostatically charged at 2.40 V for the dissolution of Li₂S into LiPS species until the charge current was lower than 0.01 mA.

Symmetric Cell Assembly and Measurements: Symmetric coin cells were prepared by assembling two identical electrodes (with an average loading of about 0.5 mg cm⁻²) as working

and counter electrodes with 40 μL of electrolyte (0.5 M Li_2S_6 and 1 M LiTFSI in 1:1 DOL/DME (v/v)). Electrodes for symmetrical cells were fabricated using the same process as electrodes for LSBs. CV tests for the symmetrical cells were performed at a scan rate of 2-40 mV s^{-1} in a voltage window between -0.8 and 0.8 V.

Results and discussion

$C_2N@NbSe_2$ composites were produced by growing $NbSe_2$ on the surface of preformed C_2N , as schematized in Figure 1 and S1. First, C_2N was prepared via a polycondensation reaction and the subsequent annealing of the product (Figure S2).^{29,30} In a second step, $C_2N@NbSe_2$ nanocomposites were produced from the reaction of Nb and Se precursors in the presence of C_2N (see experimental section for details).

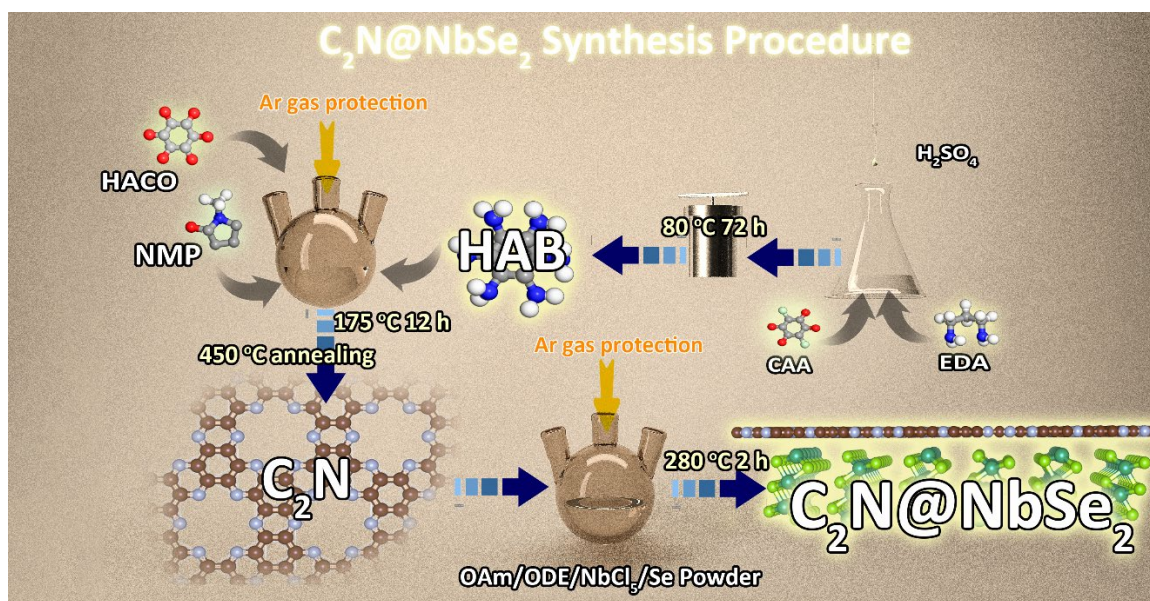


Figure 1. Schematic illustration of the synthetic procedure used to produce $C_2N@NbSe_2$ nanosheets.

Figures 2a and S3 display the 2D nanosheet geometry of the $NbSe_2$ produced in the absence of C_2N . Figure 2b and 2c show SEM and TEM images of the $C_2N@NbSe_2$ composites, which also display a 2D architecture formed by ultrathin sheets. Nitrogen adsorption-desorption isotherms (Figure S6) allowed calculating a BET specific surface area of $785 \text{ m}^2 \text{ g}^{-1}$ for $C_2N@NbSe_2$, which is a huge value taking into account the relatively high density of $NbSe_2$. XRD patterns from $C_2N@NbSe_2$ displayed the presence of the characteristic hexagonal $NbSe_2$ diffraction peaks (JCPDS No.18-0921) and a broad band at 26.2° that is assigned to C_2N (Figure 2f).^{26,29} Extensive HRTEM analysis displayed the ubiquitous presence of C_2N and $NbSe_2$ electron diffraction patterns, pointing at a nanometer-scale homogeneous distribution of both structures throughout the whole composite (Figure 2d). Additional EELS elemental maps

confirmed Nb, Se, N and C to be homogeneously distributed within the $C_2N@NbSe_2$ nanosheets (Figure 2e). The very small thickness of the sheets and the pieces of evidence showing the presence of both $NbSe_2$ and C_2N throughout the whole material pointed at a sandwich-like $C_2N@NbSe_2$ structure with $NbSe_2$ crystals grown on the surface of C_2N nanosheets. In such a configuration, with highly conductive C_2N in intimate contact with $NbSe_2$, a simultaneous high electrical conductivity, high surface area and boosted capture and catalytic conversion of LiPS is to be expected.³²

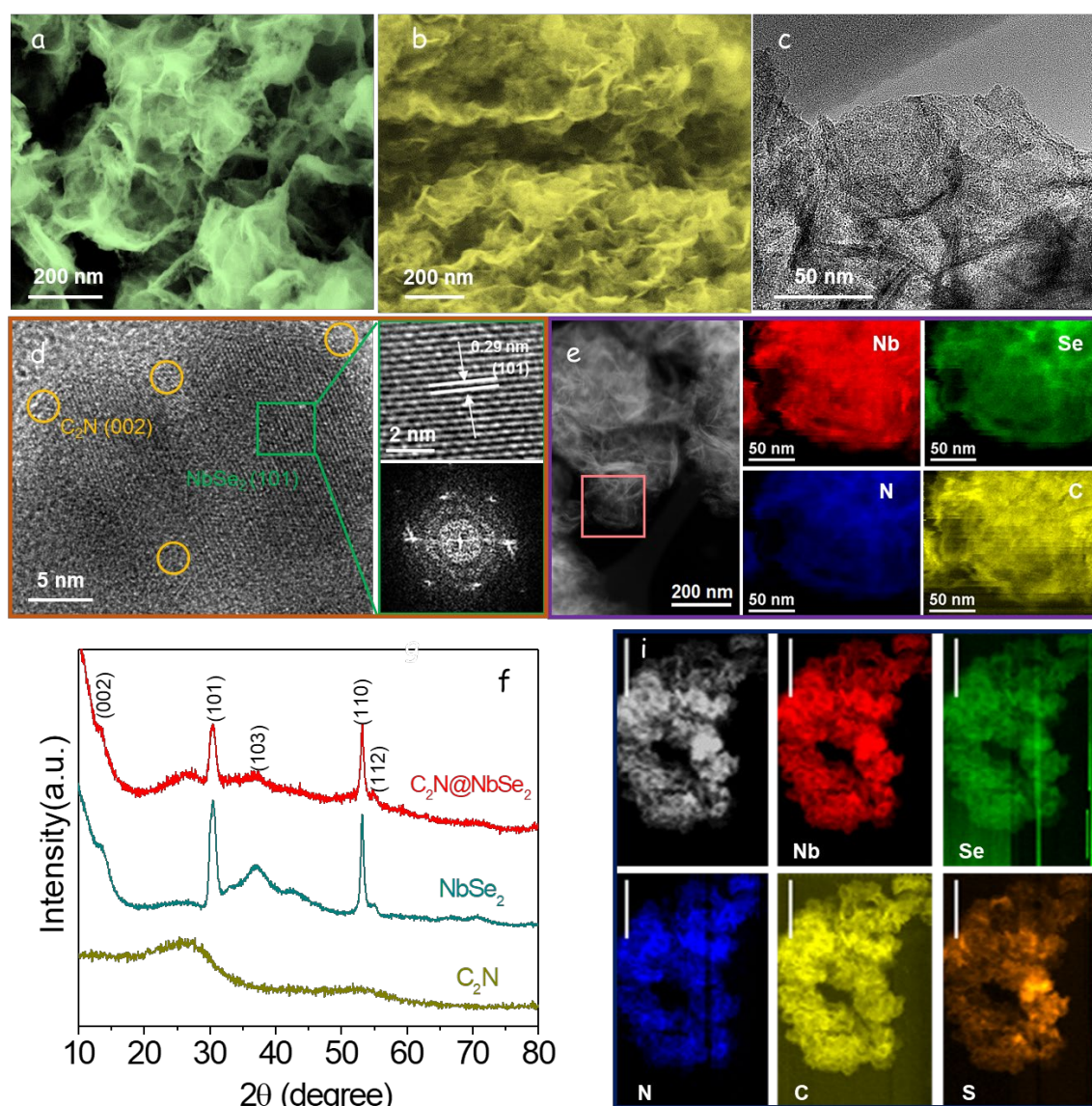


Figure 2. (a,b) SEM images of (a) $NbSe_2$ and (b) $C_2N@NbSe_2$. (c) TEM image of $C_2N@NbSe_2$. (d) HRTEM image of $C_2N@NbSe_2$ and FFT spectrum of the enlarged image of the green frame showing lattice fringes at a distance of 0.29 nm, corresponding to the (101) plane of hexagonal

NbSe₂. (e) EELS chemical composition maps obtained from the red squared area in the STEM micrograph. Individual Nb M-edge 1020 eV (red), Se L-edge 1436 eV (green), N K-edge 401 eV (blue) and C K-edge 284 eV (yellow). (f) XRD patterns of C₂N, NbSe₂ and C₂N@NbSe₂. (g) EELS chemical composition maps obtained from the STEM micrograph of a C₂N@NbSe₂/S composite. Individual Nb M-edge 1020 eV (red), Se L-edge 1436 eV (green), S L-edge 165 eV (orange), N K-edge 401 eV (blue) and C K-edge 284 eV (yellow). Vertical scale bar = 100 nm.

To further reveal the elemental composition and chemical bonding states of the as-synthesized C₂N@NbSe₂, XPS measurements were carried out (Figure S4a). The high-resolution C 1s XPS spectrum (Figure S4b) was fitted using four bands. The main band, at 284.6 eV, was associated to C-C bonds and it was used as a reference. The N 1s XPS spectrum (Figure S4c) displayed two bands at 399.6 and 406.6 eV, which can be assigned to pyrazine-like and oxidized N, respectively.^{33,34} The Nb 3d XPS spectrum (Figure S4d) presented two main peaks at 207.0 eV (3d_{5/2}) and 209.8 eV (3d_{3/2}) that were assigned to a Nb⁴⁺ chemical environment.³⁵ The binding energy of the main component in the Se 3d XPS spectrum, at 55.1 eV (3d_{5/2}), is also consistent with Se²⁻ within a metal selenide environment (Figure S4e).^{35,36} The valence band XPS spectra showed the Fermi level to lay within a band of states, thus demonstrating the metallic character of the produced composite (Figure S4f).

Sulfur was introduced within C₂N@NbSe₂ via a melt-diffusion process (see the experimental section for details). SEM characterization of the obtained C₂N@NbSe₂/S composites displayed the nanosheet-based structure of the C₂N@NbSe₂ to be conserved but to be filled with S (Figure S5a). Independent sulfur agglomerates, outside the C₂N@NbSe₂ host, were not observed after processing the material with a CS₂ solution (see details in experimental section). Figure S5b displays the XRD pattern of C₂N@NbSe₂/S, showing the presence of the cubic sulfur crystal structure (JCPDS No. 08-0247).^{22,37} STEM and EDX compositional maps further demonstrated the homogeneous loading of sulfur within C₂N@NbSe₂ composites (Figure 2g). The amount of sulfur was quantified using TGA at ca. 70.3 wt% (Figure S5c). Besides, nitrogen adsorption-desorption isotherms (Figure S6) showed the BET specific surface area of the material to be reduced with the sulfur introduction, from the initial 785 m² g⁻¹

obtained for C₂N@NbSe₂ to 21.58 m² g⁻¹ for C₂N@NbSe₂/S. Simultaneously, the pore volume decreased from 0.29 to 0.05 cm³ g⁻¹ with the loading of sulfur.

To evaluate the LiPS adsorption potential of C₂N@NbSe₂ and the different reference materials (Super P, NbSe₂, C₃N₄ and C₂N), they were immersed in a solution containing Li₂S₄ (Figure 3a). After overnight adsorption, the original orange-brown color of the Li₂S₄ solution containing Super P remained unchanged and the reference solution containing C₃N₄ became just slightly lighter. On the contrary, the color of the Li₂S₄ solutions containing either C₂N@NbSe₂, NbSe₂ or C₂N almost fully disappeared pointing at the total Li₂S₄ adsorption on the host materials. This result suggested a strong chemical interaction of LiPS with NbSe₂ and C₂N. Beyond visual inspection, the amount of Li₂S₄ in solution could be followed using UV-vis absorption spectroscopy (Figure 3b).^{38,39} The Li₂S₄ absorption band in the 400–500 nm region was observed to fully disappear from the UV-vis spectra obtained from the solutions containing C₂N, NbSe₂ or C₂N@NbSe₂.

XPS analyses were conducted to further evaluate the chemical interactions between C₂N@NbSe₂ and LiPS. Figure 3c exhibits the high-resolution N 1s XPS spectrum of C₂N@NbSe₂ before and after the Li₂S₄ adsorption test. After Li₂S₄ adsorption, N 1s bands appeared clearly shifted to higher binding energies with respect to the original N 1s spectrum. This shift is associated to the binding between N heteroatoms in C₂N with Lewis acid character and Li atoms in Li₂S₄ having a Lewis base character.²² Figure 3d shows the high-resolution Nb 3d XPS spectrum of NbSe₂@C₂N after and before Li₂S₄ adsorption test. Compared with the original Nb 3d spectrum, after Li₂S₄ adsorption Nb 3d bands also shifted to higher binding energies, which we associate with the chemical interaction between Nb and sulfur.²³

DFT calculations were used to evaluate the interaction between LiPS and C₂N@NbSe₂. First, we studied the interaction of LiPS with C₂N. The optimized adsorption configuration of six LiPS species at different lithiation stages (Li₂S, Li₂S₂, Li₂S₄, Li₂S₆, Li₂S₈ and S₈) on the C₂N surface are displayed in Figure S7. Figure 3f shows the stable adsorption configurations of Li₂S₄, which is immobilized by Li-N bonds on the C₂N surface with a binding energy of -2.86 eV. The stable geometrically configurations of LiPS species adsorbed at (001), (101) and (110) facets of NbSe₂ are illustrated in Figure S8, S9 and S10. The calculated E_b for the geometrically configurations of Li₂S₄-NbSe₂ on NbSe₂ (001), (101) and (110) surfaces were -2.66 eV, -5.76

eV and -4.32 eV (Figure 3e), respectively, demonstrating a strong LiPS chemisorption through the formation of Nb-S bonds.^{41,42} Considering the complete composite, C₂N@NbSe₂, DFT calculations demonstrated even higher binding energies with LiPS species, as detailed in Figure 3g. Overall, DFT results suggest a strong affinity of C₂N toward various LiPS species, higher than graphitic carbon,⁴⁰ a strong affinity with NbSe₂ and even a stronger affinity for the surface of these two materials when forming a heterojunction. Results also revealed that S and Li atoms in Li₂S₄ prefer to bond with Nb and N atoms on NbSe₂ and C₂N surfaces, respectively, which is consistent with results from XPS analysis.

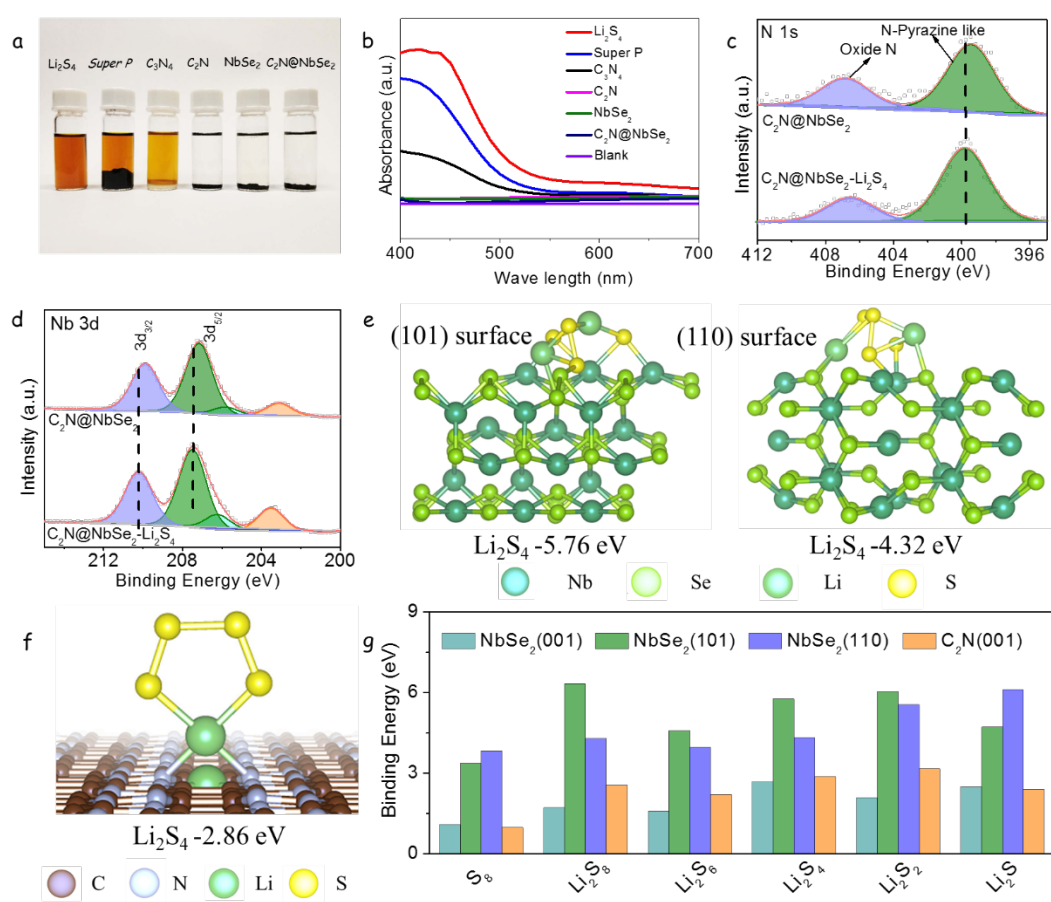


Figure 3. (a) Optical photograph of the flask containing a Li₂S₄ solution and the different adsorbents (as indicated in the image) after 12h adsorption tests. (b) UV-Vis spectra of the polysulfide solution after exposure to the different adsorbents. (c) N 1s and (d) Nb 3d XPS spectra of C₂N@NbSe₂ before and after adsorption of Li₂S₄. (e) Optimized geometrical configurations of NbSe₂ with Li₂S₄ on (101) and (110) surfaces. (f) Adsorption configurations for Li₂S₄ on C₂N surface. (g) Binding energies for LiPS (Li₂S, Li₂S₂, Li₂S₄, Li₂S₆, Li₂S₈ and S₈) on NbSe₂ and C₂N surfaces within C₂N@NbSe₂, as calculated by DFT.

DFT calculations were used to determine the C_2N - $NbSe_2$ configuration, its band structure and its affinity to polysulfides (Figure 4). The optimized geometry suggested that Nb-terminated sites of $NbSe_2$ are favorable for combining with N of C_2N , rather than Se-terminated (Figure 4b). $C_2N@NbSe_2$ showed no gap of states at the Fermi level, like $NbSe_2$, which was consistent with its metallic character and XPS data (Figure 4a). The electronic distribution within $C_2N@NbSe_2$ was analyzed by DFT charge density difference (Figure 4c). In this regard, the electron cloud around N atoms is much larger than that around Nb atoms, indicating electrons to be transferred from $NbSe_2$ to C_2N . This result showed an enhance electron mobility in the composite owing to the charge redistribution, and also explained the enhanced interaction between LiPS species and $NbSe_2$, due to the higher electronegativity of Nb atoms within the composite. DFT calculations not only confirmed the large affinity of $C_2N@NbSe_2$ to polysulfides but also demonstrated this composite to have a high potential electrocatalytic activity. Figure 4d exhibits the initial state, transition state and final state of Li_2S decomposition on $C_2N@NbSe_2$ and C_2N . The calculated energy barrier for Li_2S decomposition on $C_2N@NbSe_2$ and C_2N surface was 0.57 eV and 1.25 eV, respectively. These results demonstrate that $C_2N@NbSe_2$ can greatly reduce the Li_2S decomposition energy barrier and enhance the redox reversibility between Li_2S and LiPS.

The S reduction pathways of both C_2N/S and $C_2N@NbSe_2/S$ cathodes were also investigated. The overall reaction based on the reversible formation of Li_2S from S_8 and Li was considered. During the discharge process, the first step involves the double reduction of S_8 with two Li^+ to form Li_2S_8 , and then Li_2S_8 undergoes further reduction, forming three intermediate LiPS, such as Li_2S_6 , Li_2S_4 , Li_2S_2 and producing Li_2S as the final product. The Gibbs free energies were calculated for the above reactions on both C_2N and $C_2N@NbSe_2$ substrates. The optimized configuration of the intermediates and their Gibbs free energy profiles are exhibited in Figure 4e. The largest increase of Gibbs free energy was obtained for the conversion from Li_2S_2 to Li_2S species, suggesting this step as the rate-limiting for the total discharge process. The free energy increase was lower for $C_2N@NbSe_2$ (0.76 eV) than for C_2N (0.84 eV), which suggested that the reduction of S is more thermodynamically favourable on $C_2N@NbSe_2$ than on C_2N substrate due to the presence of $NbSe_2$.

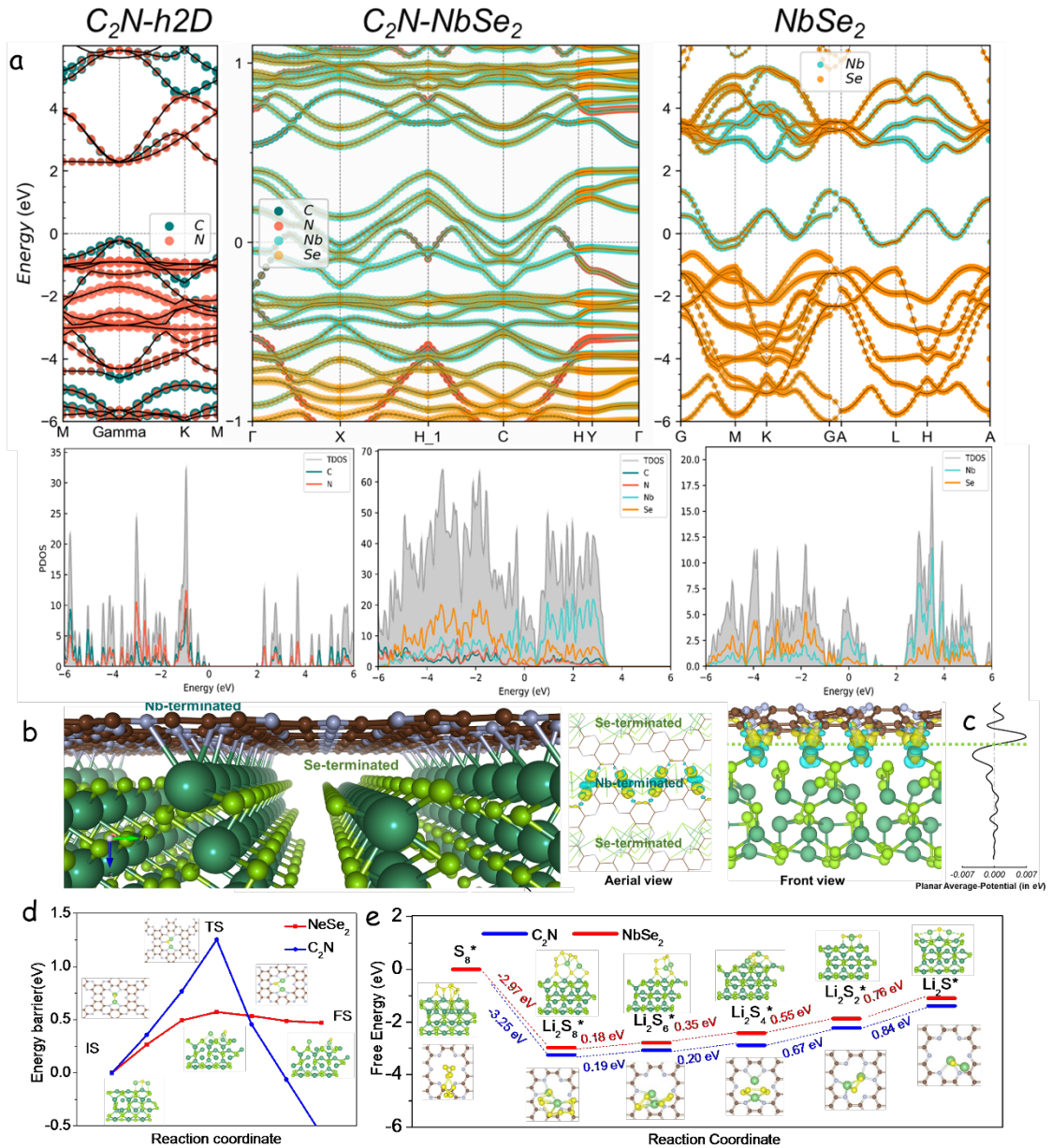


Figure 4. (a) HSE06 band structure and density of states of C₂N, NbSe₂ and C₂N@NbSe₂, respectively. (b) Optimized geometry of a C₂N-NbSe₂ heterojunction (c) Calculated charge density difference of C₂N@NbSe₂ on the (101) surface. (d) Energy barrier profiles of Li₂S cluster decomposition on C₂N and NbSe₂ along with different reaction coordinates. The initial, transition, and final structures are also displayed. The black, yellow, green, pink, and dark blue balls represent C, S, Li, N, and Co atoms, respectively. (e) Gibbs free energy profiles of LiPS species on NbSe₂ and C₂N, showing a much lower reaction free energy from Li₂S₂ to Li₂S on NbSe₂ than that on C₂N. The optimized adsorption conformation of LiPS species on NbSe₂ and C₂N also displayed.

To analyze the electrocatalytic activity of C₂N@NbSe₂-based electrodes toward polysulfide conversion, first CV on symmetric cells was performed in a voltage window of -0.8 to 0.8 V and with 0.5 mol L⁻¹ Li₂S₆ as electrolyte (Figure 5a). C₂N@NbSe₂ exhibited two reduction peaks at 0.05 and -0.28 V, and two well-defined oxidation peaks at -0.05 and 0.28 V. These peaks are associated with the following forward and reverse chemical reactions:^{37,43}



CV curves of symmetric cells with NbSe₂- and C₂N-based electrodes displayed lower peak current densities compared with C₂N@NbSe₂-based electrodes, pointing at a higher redox activity of the later. CV curves of C₂N@NbSe₂ electrodes in a Li₂S₆-free electrolyte presented the characteristic rectangular shape of a pure capacitive contribution (Figure S11a). Figure S11b shows 100 consecutive CV cycles of symmetric cells based on C₂N@NbSe₂ demonstrating good stability. CV profiles of symmetric cells with C₂N@NbSe₂ electrodes at different scanning rates showed the redox peaks to be clearly defined and to maintain a small potential gap, further demonstrating a fast polysulfide conversion kinetics and good electrochemical stability (Figure 5b).

Results from the electrochemical impedance spectroscopy (EIS) analysis of the different electrodes and the equivalent circuit used to model the symmetric cells are displayed in Figure 5c. The semicircle in the high-frequency region corresponds to the charge transfer resistance (R_{ct}) at the electrode/polysulfide interface.^{24,45} The intersection of the Nyquist plots with the abscissa is ascribed to the interphase-contact resistance of the electrolyte and the cells (R_s). The fitting of the Nyquist plots (Figure S12) showed C₂N@NbSe₂ cells to be characterized by significantly lower R_{ct} (13.5 Ω) than NbSe₂ (38.1 Ω) and C₂N (76.8 Ω), which demonstrated a significantly faster charge transfer at the C₂N@NbSe₂/polysulfide interface.

The electrochemical performance of Li-S coin cells based on the cathode materials here developed and a lithium anode was subsequently tested. Figure 5d shows the CV profiles of C₂N@NbSe₂/S, NbSe₂/S and C₂N/S cathodes at a scan rate of 0.1 mV s⁻¹. S/C₂N@NbSe₂ cathodes displayed two well-defined cathodic peaks associated with the reduction of solid-state sulfur into soluble long-chain LiPS (Li₂S_x, 4 < x < 8, peak I) and the subsequent conversion to insoluble Li₂S₂/Li₂S (peak II).⁴¹ The anodic peak (peak III) corresponds to the reverse oxidation

conversion from Li_2S to LiPS and ultimately to sulfur.^{46,47} The voltage between the second cathodic and anodic peaks is 0.25 V for cells based on a $\text{C}_2\text{N@NbSe}_2/\text{S}$ cathode, clearly below the 0.30 V and 0.39 V polarizations obtained from NbSe_2/S and $\text{C}_2\text{N}/\text{S}$ cathodes, respectively. $\text{C}_2\text{N@NbSe}_2/\text{S}$ cathodes presented a more positive potential of cathodic peaks (peak I at 2.311 and peak II at 2.051 V) and more negative anodic peak (peak III at 2.325 V) than NbSe_2/S and $\text{C}_2\text{N}/\text{S}$ (Figure 5g). To quantify the electrocatalytic activity, the onset potential at a current density of $10 \mu\text{A cm}^{-2}$ beyond the baseline current was determined (Figures S14 and 5g).^{42,49} Cells based on $\text{C}_2\text{N@NbSe}_2/\text{S}$ cathodes showed the highest onset potentials of cathodic peaks and the lowest for the anodic peak which further points out the accelerated redox kinetics obtained through the synergistic combination of these two materials. Tafel plots clearly show $\text{C}_2\text{N@NbSe}_2/\text{S}$ cathodes to deliver higher exchange current densities in the lithiation/delithiation process than NbSe_2/S and $\text{C}_2\text{N}/\text{S}$ cathodes (Figure 5e,f), also a consequence of the enhanced redox reaction kinetics of LiPS in the former.⁴⁸ Besides, the redox peaks of successive CV curves measured from $\text{C}_2\text{N@NbSe}_2/\text{S}$ cathodes almost overlapped, demonstrating good reversibility of the sulfur redox reactions (Figure S13).

The electrode reaction kinetics and the lithium-ion diffusion properties of $\text{C}_2\text{N@NbSe}_2/\text{S}$, NbSe_2/S and $\text{C}_2\text{N}/\text{S}$ cathodes were evaluated by CV tests at different sweep rates, from 0.1 to 0.4 mV s^{-1} . Figure S15 displays the increase of the peak current density and the shift of the redox peaks when increasing the scan rate. At all scan rates, $\text{C}_2\text{N@NbSe}_2/\text{S}$ -based cells exhibited the highest redox peak current and lower polarization, a consequence of the faster LiPS conversion and lower redox energy barriers (Figure S15). Both cathodic and anodic peak currents showed a linear dependence on the square root of the scanning rate, pointing at a diffusion-limited process. Therefore, the diffusion constant of lithium ions (D_{Li^+}) could be calculated using the classical Randles–Sevcik equation:^{17,50}

$$I_p = (2.69 * 10^5) n^{1.5} A D_{\text{Li}^+}^{0.5} C_{\text{Li}^+} \nu^{0.5}$$

where I_p is the peak current density, n is the number of charges transferred, A is the geometric area of the electrode, C_{Li^+} is the concentration of lithium ions in the cathode, and ν is the scan rate. As shown in Figure S16, for all redox peaks the slopes of I_p vs. $\nu^{0.5}$ obtained from $\text{C}_2\text{N@NbSe}_2/\text{S}$ cathodes were significantly higher than those obtained for the two reference electrodes, pointing at a fastest lithium-ion diffusion. Based on the Randles–Sevcik equation,

C₂N@NbSe₂/S electrodes were characterized by a D_{Li^+} at peaks I, II, and III of 3.29×10^{-7} , 4.73×10^{-7} , and 6.68×10^{-7} cm² s⁻¹, respectively, well above the values obtained for NbSe₂/S and C₂N/S (Figure S17). We assigned the higher lithium-ion diffusivities measured in C₂N@NbSe₂/S to the improved catalytic activity to accelerate LiPS conversion and to the effective LiPS trapping that blocks shuttle effect and prevents the deposition of an insulating layer.

The Li₂S nucleation and dissolution processes were further analyzed to investigate the liquid-solid reaction kinetics (see experimental section for details). As shown in Figure 5h, NbSe₂@C₂N electrodes exhibited a higher Li₂S precipitation capacity (303.5 mAh g⁻¹) compared with NbSe₂ (238.2 mAh g⁻¹) and C₂N electrodes (115.6 mAh g⁻¹). NbSe₂@C₂N electrodes were also characterized by the shortest Li₂S nucleation and growth times. The constant of Li₂S nucleation and growth can be calculated according to the following equation:⁴¹

$$Ak^2 = \frac{2}{\pi t_m^3}$$

where A is the nucleation rate constant, k is the growth rate, t_m is peak-current-corresponding Li₂S precipitation time. Higher Ak^2 values are associated with faster Li₂S nucleation and growth. As shown in Figure 5i, the Ak^2 of C₂N@NbSe₂ was 3 times and 5.5 times larger than in NbSe₂ and C₂N, respectively. These result suggested that the combination of C₂N and NbSe₂ within C₂N@NbSe₂ heterostructures significantly lower the energy barrier for Li₂S nucleation and accelerates the Li₂S precipitation kinetics.^{47,51}

Potentiostatic charge tests were carried out to study the kinetics of the Li₂S dissolution. As displayed in Figure S18, C₂N@NbSe₂ electrodes delivered higher current densities with higher capacity of Li₂S dissolution (608 mAh g⁻¹) compared with NbSe₂ (452 mAh g⁻¹) and C₂N electrodes (386 mAh g⁻¹). This result indicates that the heterostructure C₂N@NbSe₂ reduces the oxidation overpotential for Li₂S dissolution.⁵² Overall, these results verified the superior electrocatalytic performance of C₂N@NbSe₂ hosts in reducing polarization and promoting redox kinetics of LiPS conversion reaction.

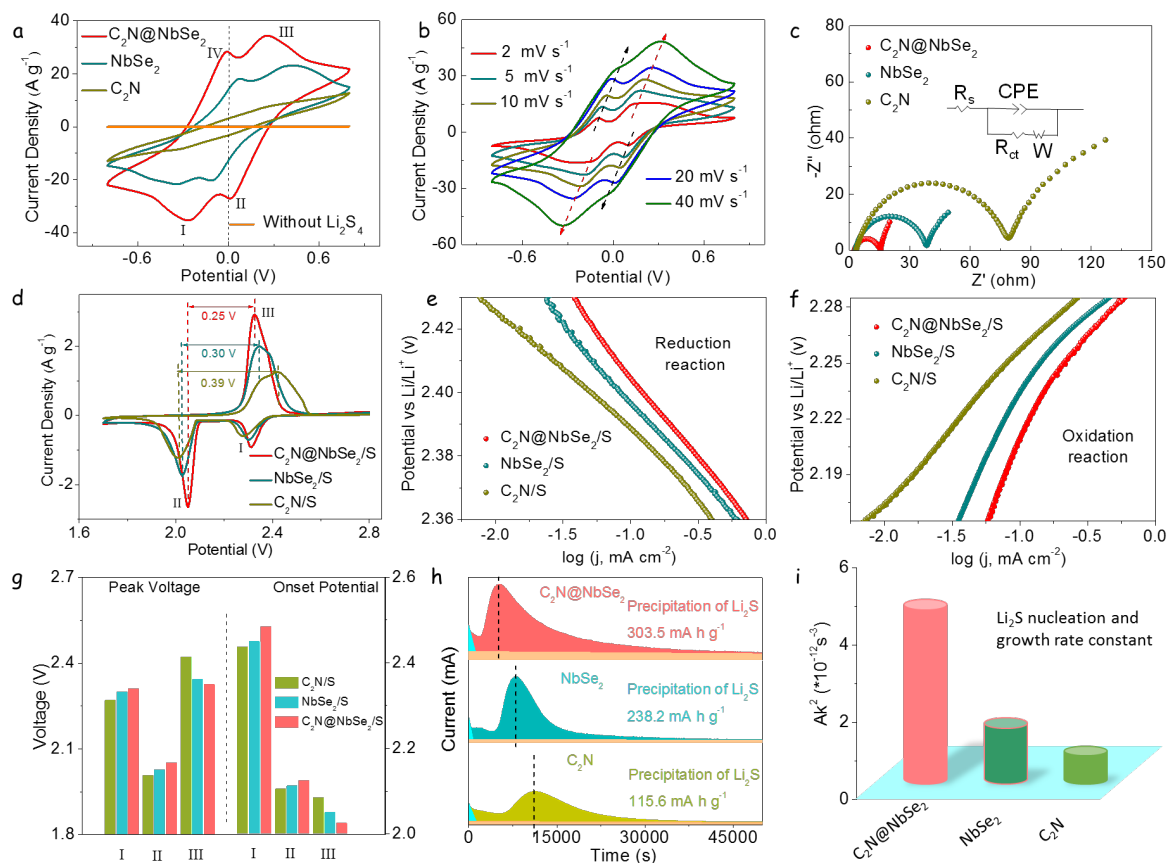


Figure 5. (a) CV curves of symmetric cells at a scan rate of $20 mV s^{-1}$. (b) CV curves of symmetric cells at different scan rates. (c) EIS curves of symmetrical cells using an electrolyte containing $0.5 mol L^{-1} Li_2S_6$. (d) CV profiles of Li-S cells with different electrodes. (e) Tafel plots of the initial lithiation process. (f) Tafel plots of the initial delithiation process. (g) Corresponding peak voltages and onset potentials of asymmetric Li-S cells. (h) Potentiostatic discharge profile at 2.05 V on different electrodes with Li_2S_8 catholyte for evaluating the nucleation kinetics of Li_2S . (i) Calculated Li_2S nucleation and growth constant.

Figure 6a shows the galvanostatic charge/discharge profiles of $C_2N@NbSe_2/S$ at various current densities, from 0.1 to 5 C ($1 C = 1672 mA g^{-1}$). Data obtained for $NbSe_2/S$ and C_2N/S are displayed in Figure S19. Galvanostatic profiles displayed two discharge plateaus and one charge plateau, consistently with CV results and the multistep sulfur reaction mechanism. The higher discharge plateau at around 2.3 V is associated with the conversion of sulfur to long-chain LiPS ($Li_2S_x, 4 \leq x \leq 8$). The lower discharge plateau at about 2.1 V ascribes to the reduction of LiPS to insoluble products (Li_2S_2/Li_2S).^{47,53} Figure S20a compares the charge/discharge profiles of

C₂N@NbSe₂/S, NbSe₂/S and S/C₂N/S electrodes at a current density of 0.1 C. The voltage gap between the second discharge and the charge plateaus is referred to as the polarization potential (ΔE). C₂N@NbSe₂/S electrodes showed a lower polarization potential ($\Delta E = 140$ mV) as compared with NbSe₂/S ($\Delta E = 194$ mV) and C₂N/S electrodes ($\Delta E = 232$ mV), as a consequence of the superior electrocatalytic activity of C₂N@NbSe₂ towards LiPS conversion.^{48,54}

Q1 and Q2 are used to refer to the capacity of the first and second discharge plateaus, respectively. The ratio Q2/Q1 can be used to evaluate the catalytic activity for LiPS conversion reaction: while Q1 is related to the ability to create soluble polysulfides, the Q2 stage reveals the amount of polysulfides reduced to Li₂S.^{22,53} Thus, the higher Q2/Q1, the better the catalytic ability. Consistently with the above results, Q2/Q1 values obtained for C₂N@NbSe₂/S electrodes (2.73) were larger than those of NbSe₂/S (2.51) and C₂N@NbSe₂/S (2.30) (Figure S20b).

Looking in more detail to the galvanostatic curves, Figure 6b displays the voltage jump at the initial charging period, which reflects the overpotential required for Li₂S activation.⁴¹ C₂N@NbSe₂/S electrodes displayed a significantly lower overpotential (25.5 mV) than NbSe₂/S (80.8 mV) and C₂N@NbSe₂/S (95.2 mV) electrodes, verifying the accelerated activation process of Li₂S in the presence of C₂N@NbSe₂. Complementarily, Figure 6c displays the voltage dip at the beginning of the Li₂S precipitation voltage plateaus in the galvanostatic discharge curves, which is associated with the overpotential for Li₂S nucleation.⁵⁵ Compared with NbSe₂/S (17.5 mV) and C₂N/S (27.1 mV) electrodes, the C₂N@NbSe₂/S electrode demonstrated a much lower overpotential for Li₂S nucleation (10.2 mV), indicating a lower energy barrier.

Figure 6d compares the rate performances of the different cells. Among the tested cathodes, C₂N@NbSe₂/S-based cells exhibited the highest rate capability with average discharge capacities of 1432, 1198, 1060, 955, 830, 746 and 683 mAh g⁻¹ at current rates from 0.1 C to 5 C, respectively. Even after switching the current density back to 0.2 C, the recovered specific capacity of C₂N@NbSe₂/S electrodes reached a similar value of 1068 mAh g⁻¹, indicating remarkable electrochemical reversibility.

Energy efficiency was calculated according to:³⁷

$$E = \int UI dt$$

As shown in Figure 6e, C₂N@NbSe₂/S delivered a higher energy efficiency compared to NbSe₂/S and C₂N/S electrodes, especially at high current densities. For instance, C₂N@NbSe₂/S-based cells displayed an energy efficiency of 87.8% at 5 C, higher than NbSe₂/S (83.5%) and C₂N/S (76.8%) cells. The significant enhancement in energy efficiency is associated with the lower polarization potential and better catalytic properties of C₂N@NbSe₂.

Galvanostatic cycling performances of cells with different cathodes are presented in Figure 6f. C₂N@NbSe₂/S cells were characterized by a remarkable initial capacity of 905 mAh g⁻¹, and maintained a capacity of 752.1 mAh g⁻¹ after 500 cycles, which corresponds to a capacity retention of 83.1%. On the other hand, after 500 cycles NbSe₂/S and C₂N/S electrodes displayed discharge capacities of 657.8 mAh g⁻¹ and 516.1 mAh g⁻¹, with a capacity retention of 75.8 % and 85.7%, respectively.

Besides, cells were disassembled to evaluate the morphology of the cathodes after cycling. As displayed in Figure S21, the C₂N@NbSe₂/S cathode material maintained its original morphology after 50 cycles, demonstrating its excellent structural stability during lithiation/delithiation processes.

Results of the EIS analysis of C₂N@NbSe₂/S, NbSe₂/S and C₂N/S cathodes after 500 cycles at 1 C are displayed in Figure 6g. The semicircle in the high-frequency region is ascribed to the deposition of the insulating discharge products of Li₂S on the electrode surface (R_d), and the second semicircle in the middle frequency region corresponds to the charge transfer resistance (R_{ct}).²² The C₂N@NbSe₂/S electrode showed a considerably lower R_d and R_{ct} compared with NbSe₂/S and C₂N/S electrodes, which is consistent with the accelerated polysulfide conversion reaction offered by the combination of the two materials, as well as by the facilitated charge transfer kinetics during lithiation/delithiation reaction.

An ultra-long cycling test was conducted for the C₂N@NbSe₂/S -based cathode at a higher current density of 3 C (Figure 6h). C₂N@NbSe₂/S-based cells delivered stable cycling life with only 0.012% capacity decay per cycle after 2000 cycles. The coulombic efficiencies of C₂N@NbSe₂/S stabilized at around 99.8%, demonstrating outstanding cycling stability. Notice, that after the initial 500 cycles, a capacity loss of just a 3.3 % was measured during the subsequent 1500 cycles.

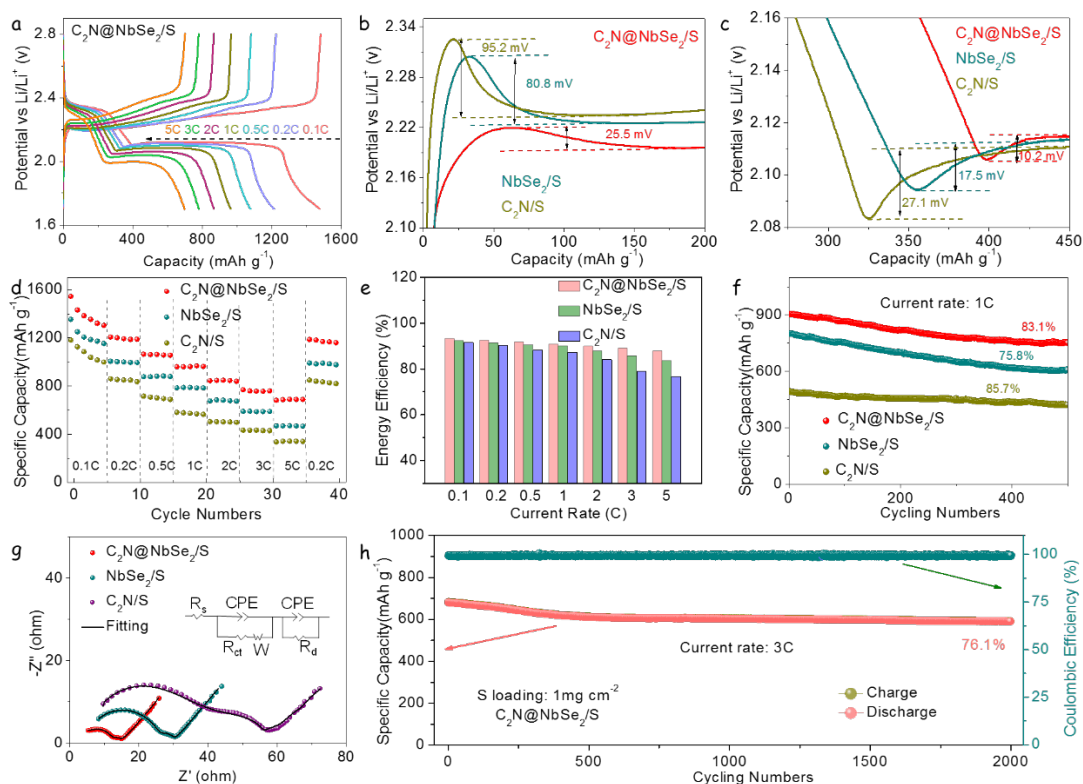


Figure 6. (a) Galvanostatic charge/discharge profiles of a $C_2N@NbSe_2/S$ electrode at various rates, from 0.1 C to 5 C ($1\text{ C} = 1672\text{ mA g}^{-1}$). (b) Charge and (c) discharge profiles of $C_2N@NbSe_2/S$, $NbSe_2/S$, and C_2N/S electrodes showing the overpotentials for conversion between soluble $LiPS$ and insoluble Li_2S_2/Li_2S . (d) Rate capability of at various C rates, from 0.1 C to 5 C. (e) Energy efficiencies at different current densities. (f) Cycling performances at 1 C. (g) Nyquist plot of EIS data from different electrodes. (h) Long cycling test of the $C_2N@NbSe_2/S$ electrode at 3 C.

To meet the high energy density requirement for LSB commercialization, the electrochemical performances of cells based on cathodes containing higher sulfur loadings was investigated. $C_2N@NbSe_2/S$ cathodes with sulfur loadings of 3.0 and 5.6 mg cm^{-2} still displayed one charge and two discharge plateaus, with a low polarization between charge and discharge processes (Figure 7a). Galvanostatic charge/discharge curves at different current rates were also measured for $C_2N@NbSe_2/S$ cathodes containing 3.0 mg cm^{-2} (Figure 7b,c) and 5.6 mg cm^{-2} of sulfur (Figure S22). $C_2N@NbSe_2/S$ cathodes delivered average areal capacities of 3.53 and 5.63 mAh cm^{-2} under sulfur loadings of 3.0 and 5.6 mg cm^{-2} , respectively. These values are in the range of the areal capacities industrially required for Li-ion battery ($\sim 4\text{ mAh cm}^{-2}$).²² Even at a

current rate of 1 C, $C_2N@NbSe_2/S$ cathodes still showed a high areal capacity of 4.01 mAh cm^{-2} when loaded with 5.6 mg cm^{-2} of sulfur. These results demonstrate the high potential $C_2N@NbSe_2/S$ cathodes to realize low polarization potentials and fast sulfur reaction kinetics even under high loading configurations. Notably, at high sulfur loadings, $C_2N@NbSe_2/S$ -based cells maintained well the voltage profile during the first 50 cycles, with just a small potential hysteresis, indicating a minor LiPS shuttling and stable sulfur electrochemistry (Figure 7d). Figure 7e presents the cycling performances of $C_2N@NbSe_2/S$ cathodes with various sulfur loading at a current of 0.2 C. The initial areal capacities were 2.84 and 4.56 mAh cm^{-2} at sulfur loadings of 3.0 and 5.6 mg cm^{-2} , respectively. After 80 cycles, high areal capacities around 2.6 and 3.7 mAh cm^{-2} were still maintained with a sulfur loading of 3.0 and 5.6 mg cm^{-2} , respectively.

Finally, to illustrate the promising practical application of LSBs based on $C_2N@NbSe_2/S$ cathodes, Figure S23 shows how a $C_2N@NbSe_2/S$ -based coin cell was used to light up a “UB”-shaped LED panel containing 23 LEDs.

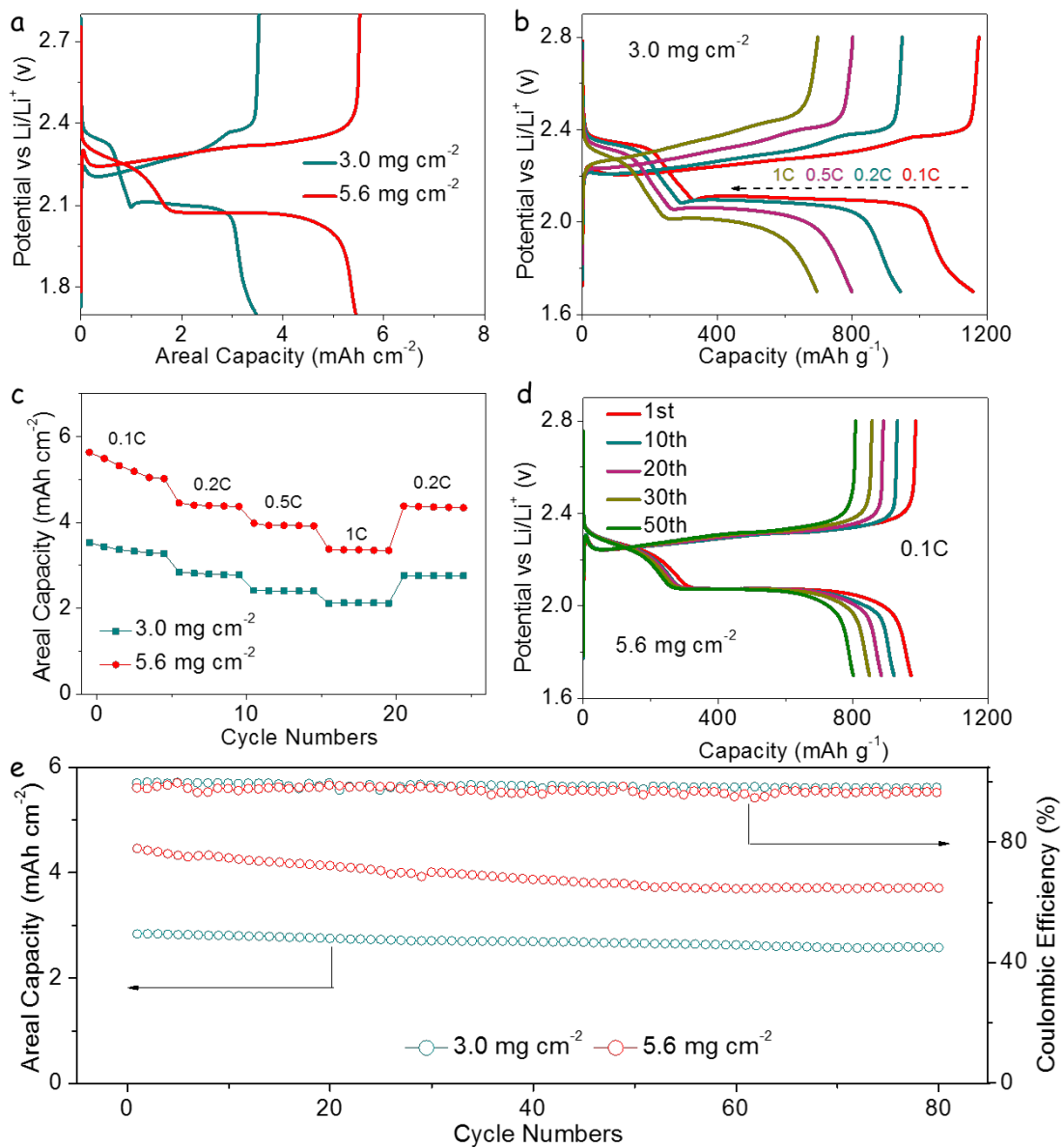


Figure 7. (a) Charge/discharge profiles at 0.1 C of $C_2N@NbSe_2/S$ cathodes with sulfur loadings of 3.0 and 5.6 $mg\ cm^{-2}$. (b) Charge/discharge profiles of $C_2N@NbSe_2/S$ cathodes at different current densities, from 0.1 C to 1 C. (c) Rate capabilities with different sulfur loadings at various current densities as indicated in the graph. (d) Galvanostatic charge/discharge profiles at 0.1 C with a sulfur loading of 5.6 $mg\ cm^{-2}$. (e) Cycling performances at 0.2 C of $C_2N@NbSe_2/S$ cathodes with different sulfur loadings.

Conclusion

In summary, we rationally designed and engineered a new and high-performance LSB cathode based on a $C_2N@NbSe_2$ sulfur host. We used a facile and effective two-step strategy to produce the composites with a nanosheet geometry that provided outstanding specific surface areas up to $785 \text{ m}^2 \text{ g}^{-1}$. The unique architecture of the sandwich-type $C_2N@NbSe_2$ nanosheets delivered a conductive framework for electron/ion transfer, a cushion to mitigate the effect of the volume variation of the sulfur cathode during cycling, and a multifunctional LiPS barrier that effectively suppressed polysulfide shuttling. We demonstrated experimentally and using DFT calculations that both C_2N and $NbSe_2$ were independently characterized by excellent LiPS adsorbability and catalytic activity towards reacting LiPS. Both, C_2N and $NbSe_2$ nanosheets enhance the redox kinetics of sulfur species, especially for the conversion between soluble LiPS species and Li_2S_2/Li_2S during charge/discharge processes. However, it was the combination of both materials within heterostructured $C_2N@NbSe_2$ that synergistically provided the best performances. $C_2N@NbSe_2$ nanosheets exhibited the largest conductivity, most robust LiPS adsorbability, and highest catalytic activity. The high current densities obtained in CV curves of symmetric cells illustrated that $C_2N@NbSe_2$ with high redox activity could accelerate reaction kinetics during liquid-to-solid ($Li_2S \leftrightarrow S_6^{2-} \leftrightarrow S_8$) conversion. The fast charge transfer at the $C_2N@NbSe_2$ /polysulfide interface demonstrated by EIS, indicated considerable enhancement on redox kinetics of polysulfides in the liquid phase by introducing highly sulfiphilic/lithiophilic sites. A high Q2/Q1 ratio provided strong evidence that $C_2N@NbSe_2$ could confine polysulfides within the cathode zone and facilitate the liquid-solid transformation from LiPS to Li_2S . Consistent with these excellent qualities, $C_2N@NbSe_2/S$ cathodes delivered exceptional long-term cycling stability with a very low capacity decay of 0.012% per cycle over 2000 cycles at 3 C, with only a total of 3.3% capacity loss in the last 1500 cycles, and exceptional rate performance of 683 mAh g^{-1} at 5 C. Moreover, $C_2N@NbSe_2/S$ cathodes delivered a high areal capacity of 5.65 mAh cm^{-2} at a sulfur loading of 5.6 mg cm^{-2} . This work not only emphasizes the potential capabilities of transition-metal selenides and particularly the so far unexplored $NbSe_2$, but also proposes a novel promising C_2N as a potential cathode material.

Acknowledgements

This work was supported by the European Regional Development Funds and by the Spanish Ministerio de Economía y Competitividad through the project SEHTOP, ENE2016- 77798-C4-3-R, and ENE2017-85087-C3. D. Yang and C. Zhang thank the China Scholarship Council for the scholarship support. Z. Liang acknowledges funding from MINECO SO FPI PhD grant (SEV-2013-0295-17-1). Authors acknowledge funding from Generalitat de Catalunya 2017 SGR 327 and 2017 SGR 1246. ICN2 acknowledges the support from the Severo Ochoa Programme (MINECO, grant no. SEV-2017-0706) and is funded by the CERCA Programme/Generalitat de Catalunya. J. Llorca is a Serra Húnter Fellow and is grateful to MICINN/FEDER RTI2018-093996-B-C31, GC 2017 SGR 128 and to ICREA Academia program. Part of the present work has been performed in the framework of Universitat Autònoma de Barcelona Materials Science PhD program. MCS have received funding from the European Union's Horizon 2020 research and innovation programme under the Marie Skłodowska-Curie grant agreement No 754510 (PROBIST). M.B. acknowledges support from SUR Generalitat de Catalunya and the EU Social Fund; project ref. 2020 FI 00103.

References

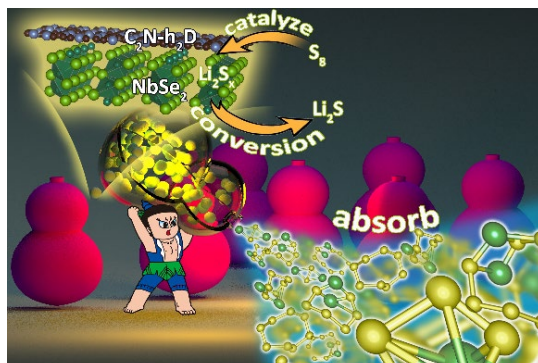
1. S. Chu, Y. Cui and N. Liu, *Nat. Mater.*, 2016, **16**, 16-22.
2. G. Zhou, D.-W. Wang, F. Li, P.-X. Hou, L. Yin, C. Liu, G. Q. Lu, I. R. Gentle and H.-M. Cheng, *Energy Environ. Sci.*, 2012, **5**, 8901.
3. S.-L. Chou and S.-X. Dou, *Adv. Mater.*, 2017, **29**, 1705871.
4. Z. W. Seh, Y. Sun, Q. Zhang and Y. Cui, *Chem. Soc. Rev.*, 2016, **45**, 5605-5634.
5. A. Manthiram, Y. Fu, S. H. Chung, C. Zu and Y. S. Su, *Chem. Rev.*, 2014, **114**, 11751-11787.
6. Z. Li, H. B. Wu and X. W. Lou, *Energy Environ. Sci.*, 2016, **9**, 3061-3070.
7. J. He, L. Luo, Y. Chen and A. Manthiram, *Adv. Mater.*, 2017, **29**, 1702707.
8. J. Schuster, G. He, B. Mandlmeier, T. Yim, K. T. Lee, T. Bein and L. F. Nazar, *Angew. Chem. Int. Ed.*, 2012, **51**, 3591-3595.
9. X.-B. Cheng, J.-Q. Huang, Q. Zhang, H.-J. Peng, M.-Q. Zhao and F. Wei, *Nano Energy*, 2014, **4**, 65-72.
10. W. Tian, B. Xi, Z. Feng, H. Li, J. Feng and S. Xiong, *Adv. Energy Mater.*, 2019, **9**, 1901896.
11. Z. Xiao, L. Li, Y. Tang, Z. Cheng, H. Pan, D. Tian and R. Wang, *Energy Storage Mater.*, 2018, **12**, 252-259.
12. J. S. Lee, W. Kim, J. Jang and A. Manthiram, *Adv. Energy Mater.*, 2017, **7**, 1601943.
13. Z. Li, J. Zhang, B. Guan, D. Wang, L. M. Liu and X. W. Lou, *Nat. Commun.*, 2016, **7**, 13065.
14. L. Hu, C. Dai, H. Liu, Y. Li, B. Shen, Y. Chen, S.-J. Bao and M. Xu, *Adv. Energy Mater.*, 2018, **8**, 1800709.
15. Z. Sun, J. Zhang, L. Yin, G. Hu, R. Fang, H. M. Cheng and F. Li, *Nat. Commun.*, 2017, **8**, 14627.
16. T. Lei, W. Chen, J. Huang, C. Yan, H. Sun, C. Wang, W. Zhang, Y. Li and J. Xiong, *Adv. Energy Mater.*, 2017, **7**, 1601843.
17. D. Cai, B. Liu, D. Zhu, D. Chen, M. Lu, J. Cao, Y. Wang, W. Huang, Y. Shao, H. Tu and W. Han, *Adv. Energy Mater.*, 2020, **10**, 1904273.
18. Q. Pang, D. Kundu and L. F. Nazar, *Mater. Horiz.*, 2016, **3**, 130-136.
19. C. Ye, Y. Jiao, H. Jin, A. Slattery, K. Davey, H. Wang and S.-Z. Qiao, *Angew. Chem., Int. Ed.*, 2018, **57**, 16703-16707.

20. Y. Tang, X. Li, H. Lv, D. Xie, W. Wang, C. Zhi and H. Li, *Adv. Energy Mater.*, 2020, **10**, 2000892.
21. Y. Hou, M. R. Lohe, J. Zhang, S. Liu, X. Zhuang and X. Feng, *Energy Environ. Sci.*, 2016, **9**, 478-483.
22. D. Yang, C. Zhang, J. J. Biendicho, X. Han, Z. Liang, R. Du, M. Li, J. Li, J. Arbiol, J. Llorca, Y. Zhou, J. R. Morante and A. Cabot, *ACS nano*, 2020, DOI: 10.1021/acsnano.0c06112.
23. Y. Tian, G. Li, Y. Zhang, D. Luo, X. Wang, Y. Zhao, H. Liu, P. Ji, X. Du, J. Li and Z. Chen, *Adv. Mater.*, 2020, **32**, e1904876.
24. P. Guo, K. Sun, X. Shang, D. Liu, Y. Wang, Q. Liu, Y. Fu and D. He, *Small*, 2019, **15**, e1902363.
25. S. Fan, S. Huang, M. E. Pam, S. Chen, Q. Wu, J. Hu, Y. Wang, L. K. Ang, C. Yan, Y. Shi and H. Y. Yang, *Small*, 2019, **15**, 1906132.
26. P. Sekar, E. Greyson, J. Barton and T. Odom, *J. Am. Chem. Soc.*, 2005, **127**, 2054 -2055.
27. J. Wu and L.-W. Wang, *J. Mater. Chem. A*, 2018, **6**, 2984-2994.
28. Y. Zheng, H. Li, H. Yuan, H. Fan, W. Li and J. Zhang, *Appl. Surf. Sci.*, 2018, **434**, 596-603.
29. S. S. Shinde, C. H. Lee, J.-Y. Jung, N. K. Wagh, S.-H. Kim, D.-H. Kim, C. Lin, S. U. Lee and J.-H. Lee, *Energy Environ. Sci.*, 2019, **12**, 727-738.
30. J. Mahmood, F. Li, S.-M. Jung, M. S. Okyay, I. Ahmad, S.-J. Kim, N. Park, H. Y. Jeong and J.-B. Baek, *Nat. Nanotechnol.*, 2017, **12**, 441-446.
31. H. Li, S. Ma, H. Cai, H. Zhou, Z. Huang, Z. Hou, J. Wu, W. Yang, H. Yi, C. Fu and Y. Kuang, *Energy Storage Mater.*, 2019, **18**, 338-348.
32. R. Li, H. Peng, Q. Wu, X. Zhou, J. He, H. Shen, M. Yang and C. Li, *Angew. Chem. Int. Ed.*, 2020, **59**, 12129–12138.
33. F. Xiao, G.-L. Xu, C.-J. Sun, M. Xu, W. Wen, Q. Wang, M. Gu, S. Zhu, Y. Li, Z. Wei, X. Pan, J. Wang, K. Amine and M. Shao, *Nano Energy*, 2019, **61**, 60-68.
34. J. Mahmood, E. K. Lee, M. Jung, D. Shin, I. Y. Jeon, S. M. Jung, H. J. Choi, J. M. Seo, S. Y. Bae, S. D. Sohn, N. Park, J. H. Oh, H. J. Shin and J. B. Baek, *Nat. Commun.*, 2015, **6**, 6486.
35. J. Zhang, C. Du, J. Zhao, H. Ren, Q. Liang, Y. Zheng, S. Madhavi, X. Wang, J. Zhu and Q. Yan, *ACS Appl. Mater. Interfaces*, 2018, **10**, 37773-37778.

36. Y. Wang, A. Chen, S. Lai, X. Peng, S. Zhao, G. Hu, Y. Qiu, J. Ren, X. Liu and J. Luo, *J. Catal.*, 2020, **381**, 78-83.
37. Zhang, J. J. Biendicho, T. Zhang, R. Du, J. Li, X. Yang, J. Arbiol, Y. Zhou, J. R. Morante and A. Cabot, *Adv. Funct. Mater.*, 2019, **29**, 1903842.
38. J. Song, Z. Yu, M. L. Gordin and D. Wang, *Nano Lett.*, 2016, **16**, 864-870.
39. X. Li, K. Ding, B. Gao, Q. Li, Y. Li, J. Fu, X. Zhang, P. K. Chu and K. Huo, *Nano Energy*, 2017, **40**, 655-662.
40. T.-Z. Hou, W.-T. Xu, X. Chen, H.-J. Peng, J.-Q. Huang and Q. Zhang, *Angew. Chem. Int. Ed.*, 2017, **129**, 8290–8294.
41. M. Wang, L. Fan, X. Sun, B. Guan, B. Jiang, X. Wu, D. Tian, K. Sun, Y. Qiu, X. Yin, Y. Zhang and N. Zhang, *ACS Energy Letter*, 2020, **5**, 3041-3050.
42. X. Liu, Q. He, H. Yuan, C. Yan, Y. Zhao, X. Xu, J.-Q. Huang, Y.-L. Chueh, Q. Zhang and L. Mai, *J. Energy Chem.*, 2020, **48**, 109-115.
43. H. Lin, L. Yang, X. Jiang, G. Li, T. Zhang, Q. Yao, G. W. Zheng and J. Y. Lee, *Energy Environ. Sci.*, 2017, **10**, 1476-1486.
44. M. Wang, Y. Song, Z. Sun, Y. Shao, C. Wei, Z. Xia, Z. Tian, Z. Liu and J. Sun, *ACS nano*, 2019, **13**, 13235-13243.
45. J. Zhou, X. Liu, L. Zhu, J. Zhou, Y. Guan, L. Chen, S. Niu, J. Cai, D. Sun, Y. Zhu, J. Du, G. Wang and Y. Qian, *Joule*, 2018, **2**, 2681-2693.
46. L. Zhang, X. Chen, F. Wan, Z. Niu, Y. Wang, Q. Zhang and J. Chen, *ACS nano*, 2018, **12**, 9578-9586.
47. S. Huang, Y. V. Lim, X. Zhang, Y. Wang, Y. Zheng, D. Kong, M. Ding, S. A. Yang and H. Y. Yang, *Nano Energy*, 2018, **51**, 340-348.
48. L. Zhang, D. Liu, Z. Muhammad, F. Wan, W. Xie, Y. Wang, L. Song, Z. Niu and J. Chen, *Adv. Mater.*, 2019, **31**, e1903955.
49. Z. Yuan, H. J. Peng, T. Z. Hou, J. Q. Huang, C. M. Chen, D. W. Wang, X. B. Cheng, F. Wei and Q. Zhang, *Nano Lett.*, 2016, **16**, 519-527.
50. G. Zhou, H. Tian, Y. Jin, X. Tao, B. Liu, R. Zhang, Z. W. Seh, D. Zhuo, Y. Liu, J. Sun, J. Zhao, C. Zu, D. S. Wu, Q. Zhang and Y. Cui, *Proc. Natl. Acad. Sci. USA* 2017, **114**, 840.

51. Y. Wang, R. Zhang, Y.-c. Pang, X. Chen, J. Lang, J. Xu, C. Xiao, H. Li, K. Xi and S. Ding, *Energy Storage Mater.*, 2019, **16**, 228-235.
52. H. Yuan, H.-J. Peng, B.-Q. Li, J. Xie, L. Kong, M. Zhao, X. Chen, J.-Q. Huang and Q. Zhang, *Adv. Energy Mater.*, 2019, **9**, 1802768.
53. D. Su, M. Cortie, H. Fan and G. Wang, *Adv. Mater.*, 2017, **29**, 1700587.
54. H. Zhang, D. Tian, Z. Zhao, X. Liu, Y.-N. Hou, Y. Tang, J. Liang, Z. Zhang, X. Wang and J. Qiu, *Energy Storage Mater.*, 2019, **21**, 210-218.
55. Z. Du, X. Chen, W. Hu, C. Chuang, S. Xie, A. Hu, W. Yan, X. Kong, X. Wu, H. Ji and L. J. Wan, *J. Am. Chem. Soc.*, 2019, **141**, 3977-3985.

Table of Contents (TOC)



Rationally designed multifunctional polysulfide mediators based on $C_2N@NbSe_2$ are demonstrated as excellent cathode materials in lithium-sulfur batteries (LSBs), realizing the adsorption-catalysis-conversion of polysulfides. Thus, LSBs batteries with exceptional lifespan are delivered.